IEEE Access
Multidisciplinary | Rapid Review | Open Access Journal

Received March 21, 2019, accepted April 4, 2019, date of publication April 15, 2019, date of current version May 1, 2019.

Digital Object Identifier 10.1109/ACCESS.2019.2911358

Automated Product Boundary Defect Detection Based on Image Moment Feature Anomaly

YEPING PENG[1], (Member, IEEE), SONGBO RUAN[1], GUANGZHONG CAO[1], (Senior Member, IEEE), SUDAN HUANG[1], (Member, IEEE), NGAIMING KWOK[2], AND SHENGXI ZHOU[3]

[1]Shenzhen Key Laboratory of Electromagnetic Control, College of Mechatronics and Control Engineering, Shenzhen University, Shenzhen 518060, China
[2]School of Mechanical and Manufacturing Engineering, The University of New South Wales, Sydney, NSW 2052, Australia
[3]School of Aeronautics, Northwestern Polytechnical University, Xi'an 710072, China

Corresponding author: Guangzhong Cao (gzcao@szu.edu.cn)

This work was supported in part by the National Natural Science Foundation of China, China, under Grant U1813212, Grant 51677120, and Grant 11802237, in part by the Natural Science Foundation of Guangdong Province, China, under Grant 2018A030310522 and Grant 2017A030310460, in part by the Shenzhen Science and Technology Planning Project, China, under Grant JCYJ20170818100522101 and Grant 20170919104246276, and in part by the Natural Science Foundation of Shenzhen University, China, under Grant 2017032.

ABSTRACT Electric distribution cabinets are critical components in the power distribution pipeline. Surface defect detection plays an important role in the production process. It not only guarantees product quality but also affects the brand reputation. In particular, the boundaries of metallic cabinets are more vulnerable to be damaged than other surface areas. Thus, boundary defect detection is a bottleneck problem that needs to be solved. To deal with this issue, a method based on image moment feature anomaly is developed to detect the defects on cabinet surfaces. The boundary edges from an image of the produced cabinet are first extracted using a hybrid of edge detection and boundary skeleton extraction. Then, the boundary areas are divided into small and identical size image blocks. A Gaussian distribution model of normal image blocks without defects is established. Finally, the anomaly features of image blocks with defects are extracted to identify the defect image blocks based on the Gaussian distribution model and a segmentation threshold. Two experiments are carried out. One is to determine the optimal illumination intensity for image acquisition and the optimal threshold of defect detection. The other is to evaluate the performance of the defect detection method. This developed approach can be applied in the non-destructive and effective inspection of electric distribution cabinets and provides a feasible solution for metallic product quality assurance.

INDEX TERMS Boundary defect detection, electric distribution cabinets, image moment, anomaly detection.

I. INTRODUCTION

External quality is one of the most important subjective quality attributes of electric distribution cabinets. The cabinets are used to place electrical components and controllers, and are usually painted to avoid metallic corrosion. The appearance of electric distribution cabinets critically affects their point-of-sale value and the buying behavior of consumers. In particular, the product boundaries, the area where two surfaces are connected, are easily damaged due to collision than other areas. Defects commonly found include scratches, pits and peeled of painting. This often causes sales return and/or consumer complaints, leading to great economic losses and corporate reputation damages. Therefore, boundary defect detection has become an important processing stage in production and quality control [1]–[3].

Traditional appearance quality inspection methods relied on manual detection are low efficient and result in high error rate [4]. Furthermore, manual detection results are sometimes inconsistent due to the influence of surrounding environment. Hence, it is necessary to develop an automatic defect detection method to replace manual inspection. To this end, machine vision technology has been widely adopted for automatic surface defect detection [5]–[8]. In the literature,

The associate editor coordinating the review of this manuscript and approving it for publication was Lefei Zhang.

existing methods can be divided into four groups: filtering approaches [9], structural algorithms [10], model-based techniques [11] and statistical methods [12], [13]. Filtering methods including wavelet transform and Gabor filter are used to remove image noise to enhance feature information that facilitates defect detection [14]. Structural methods such as morphological operations and edge detection are often employed to detect defects by utilizing the product texture information [15]. Model-based techniques establish an identification algorithm of defect detection by utilizing the hidden Markov model and autoregressive model [16]. Statistical methods, such as histogram, co-occurrence matrix and autocorrelation function, are applied to construct the gray level distribution of image pixels to acquire defect information [17].

However, most of the above methods are focused on surface defect detection and have not considered the defects on product boundaries, which is still a challenge for quality control in automatic production. Aiming at detecting defects on the boundaries of electric distribution cabinets, this paper presents a method of boundary defect detection based on image moment feature anomaly. Image enhancement and sharpening are firstly implemented by utilizing the Gaussian smoothing filter and the Sobel gradient operator to mitigate the interference of uneven illumination. Then the boundary area is separated from the cabinet surface based on threshold segmentation. In this stage, the K3M tinning algorithm is employed to extract the cabinet boundary skeleton to acquire precise boundary locations. Afterwards, the segmented boundary area is divided into separate blocks that are used as defect detecting samples. By doing so, the Gaussian distribution model based anomaly detection method is established to identify the image blocks with defects. This work provides a practical method of boundary defect detection for quality inspection in automatic industrial production applications.

The rest of the paper is organized as follows. A description of the defect detection system is given in Section II. Section III details the boundary extraction procedure. Defect detection based on image moment feature anomaly is presented in Section IV. Experiments are described and results are discussed in Section V. Conclusions are given in Section VI.

II. VISION-BASED ELECTRICAL CABINET SURFACE INSPECTION SYSTEM

Figure 1 shows the schematic diagram of the vision inspection system for electric distribution cabinet surface defect detection. The target detection area on the cabinet is treated separately as a surface and its boundaries. Accordingly, appearance quality inspection of the cabinet are carried out for surface defect detection and boundary defect detection. In the work reported in [18], cabinet complex surface defect detection has been accomplished. The current work aims to tackle the problem of boundary defect inspection. Two industrial cameras with field-of-view of 1.0m × 1.2m (width × height) and resolution of 2478 × 3840 pixels are

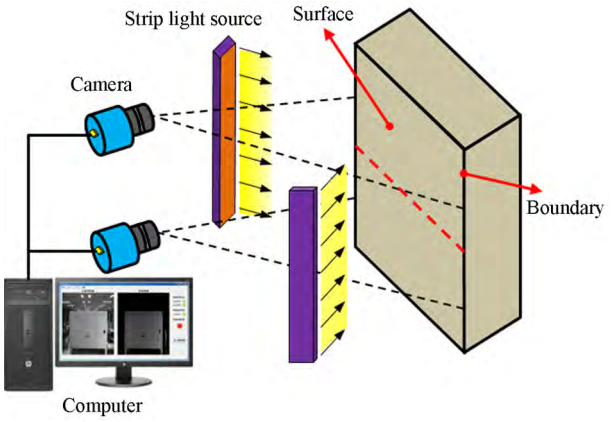

FIGURE 1. Schematic diagram of a vision inspection system for electric distribution cabinet surface defect detection.

used to capture images of the cabinet surface of 0.6m × 1.6m in size. In order to effectively capture the contour of boundary regions, two strip light sources are used to illuminate the surface and they are mounted in parallel to the vertical boundaries. The captured images are transmitted to a computer for boundary defect detection.

Despite two cameras are needed to capture the large size (0.6m × 1.6m) cabinet surface, the image processing procedures for the two cameras are the same. Hence, only the boundary defect detection process on the upper cabinet area (0.6m × 0.8m) is described, as shown in Figure 2(a). Because two parallel strip sources are used to illuminate the cabinet surface, the gray distributions of the horizontal and vertical boundary areas are different. Figures 2(b) and 2(c) display the gray distributions of "A" and "B" regions marked with green and yellow in Figure 2(a). It can be found that gray values of the boundary area in region "A" change slowly from 0 to 58, however, these in region "B" sharply increase to 120 and then decrease to 70. Because of this phenomenon, it needs to treat defect detection separately on the horizontal and vertical boundaries, and the process will be detailed in the next section.

III. BOUNDARY EDGE DETECTION

In order to detect defects on product boundaries, the boundary areas should be firstly extracted to avoid the influence of neighboring surface morphology. Figure 3 shows the flowchart of the boundary extraction process. The cabinet surface image, Figure 2(a), is used as input. A high-pass filter [19] is applied to limit the influence of the low frequency surface texture. Moreover, a gradient sharpening algorithm [20] is employed to sharpen the image. Then the region of interest (ROI) on the boundary area is extracted by combing threshold segmentation and morphological erosion. Afterwards, as mentioned above, the horizontal and vertical boundaries are separately processed because of their different gray value distributions. For vertical boundary extraction, the sharpened image after high-pass filtering is integrated with the ROI of vertical boundary area to obtain its boundary

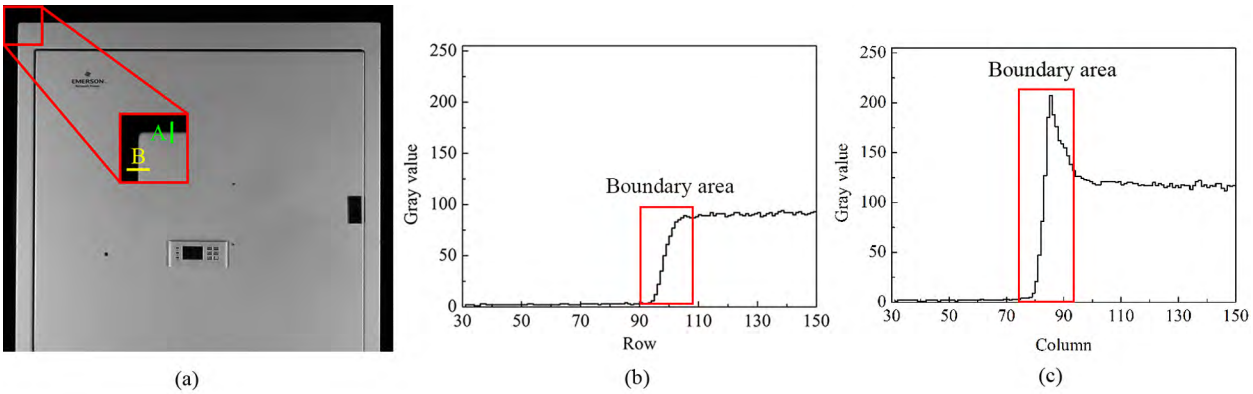

FIGURE 2. Cabinet image and gray distributions of the marked areas: (a) cabinet surface image, (b) gray distribution of A, and (c) gray distribution of B.

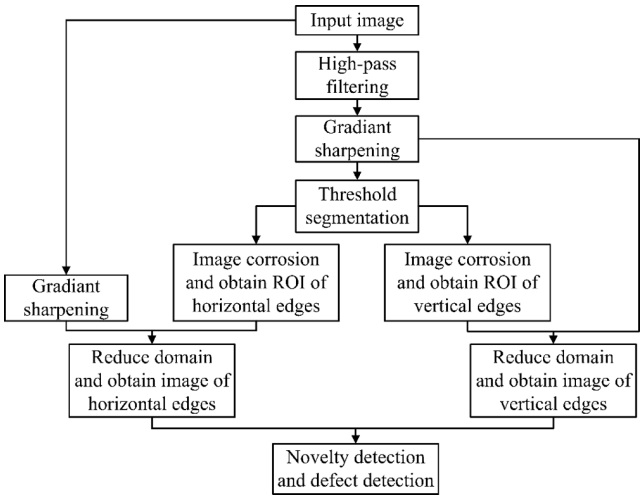

FIGURE 3. Flowchart of boundary extraction.

skeleton. Due to the slow change of horizontal boundary gray values, as shown in Figure 2(b), it does not need to filter the low frequency information but needs to enhance the gray gradient of the input image. Therefore, the input image is sharpened and integrated with the ROI of horizontal boundary area, and the horizontal boundary skeleton extraction is achieved.

The purpose of image gradient sharpening is to facilitate image edge extraction. There are many operators, such as Roberts, Laplace, Prewitt, Sobel and Kirsch operators, which can be applied to produce image edges, and their processing results on the cabinet image are shown in Figure 4. It can be seen that edge detection results obtained from Roberts, Kirsch and Laplace operators show some unwanted artifacts caused by uneven illumination and surface texture features. The Prewitt and Sobel operation results are satisfactory, and the Sobel operator will be used for edge detection in this work.

Further Sobel-based edge detection results for product boundary edges are shown in Figure 5. Considering that the boundary edge is the largest size compared with other pattern edges, image erosion operation is employed to remove the surface pattern edges. Then image dilation operation is applied to extract the boundary edge, which is the so-called boundary ROI. Based on this, the vertical and horizontal boundaries are obtained.

However, the edge detection results are not the actual boundary areas. In order to ensure accurate defect detection on boundaries, the boundary ROI needs to be further processed to acquire precise boundary locations. For this purpose, the boundary skeleton [21] is acquired by thinning the detected edges to be lines only with a single pixel width. Figure 6 shows the thinned results processed with the one-pass thinning algorithm (OPTA) [22], K3M tinning algorithm [23] and Zhang-Suen tinning algorithm [24]. The three processed results are similar. The K3M algorithm is selected as the cabinet boundary skeleton extraction method because of its computation efficiency [23].

It can also be seen in Figure 6 that the boundary skeleton is not a straight line due to the influence of image noise and/or surface defects. For a regular shape object, the line fitting methods are used to straighten the boundary skeleton lines. Figure 7 shows the fitting results obtained with the Hough transform (HT) [25], the least squares (LS) [26], the Huber-weighted least squares (HWLS) [27] and the Bisquare-weighted least squares (BWLS) [28] methods. From the enlarged figure, it can be seen that the fitted line of boundary skeleton using the BWLS algorithm is most effective as compared with other three processes. Finally, the BWLS fitting line is integrated with image gradient sharpening to extract cabinet boundary images.

IV. BOUNDARY DEFECT DETECTION BASED ON IMAGE MOMENT FEATURE ANOMALY

Boundary defect detection can be performed based on the segmentation of cabinet boundary image. This work aims to determine whether the product boundary has defects instead of identifying the types of defect. Hence, image moment features are suggested as indicators of defects, and anomaly

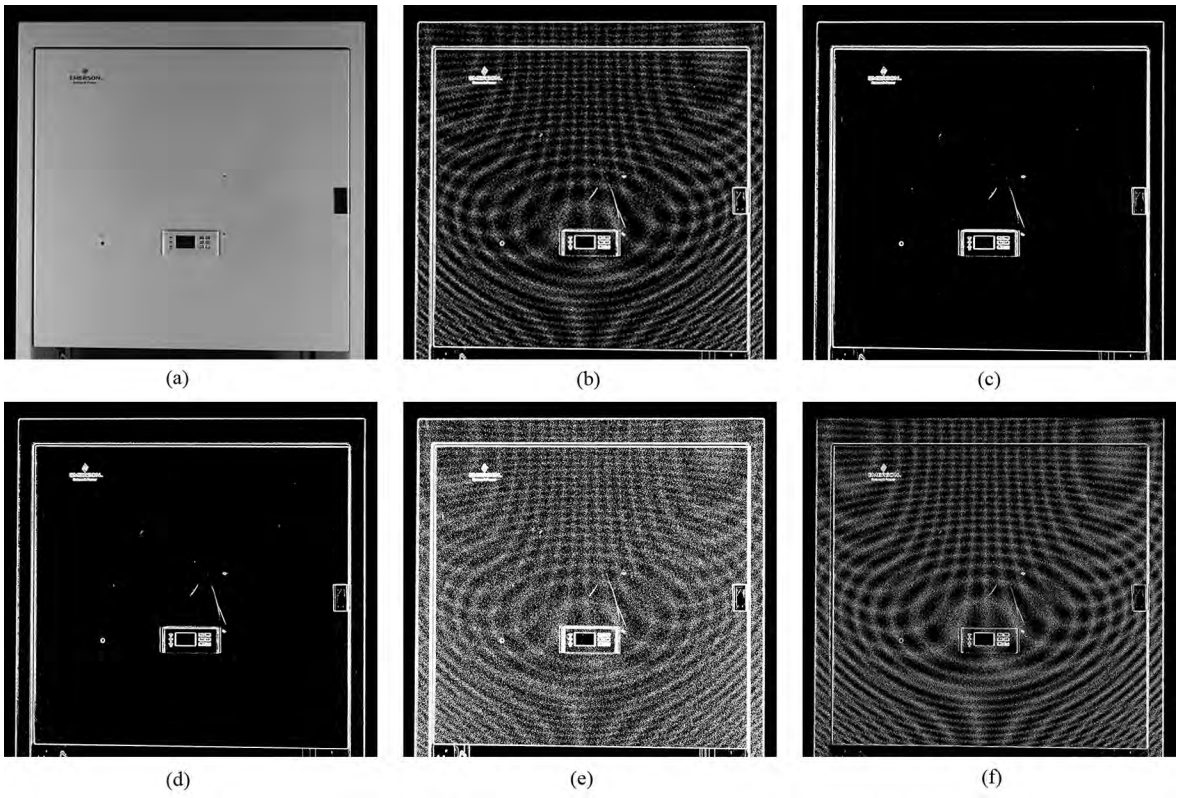

FIGURE 4. Edge detection results using different operators: (a) gray image, (b) Roberts, (c) Prewitt, (d) Sobel, (e) Kirsch, and (f) Laplace.

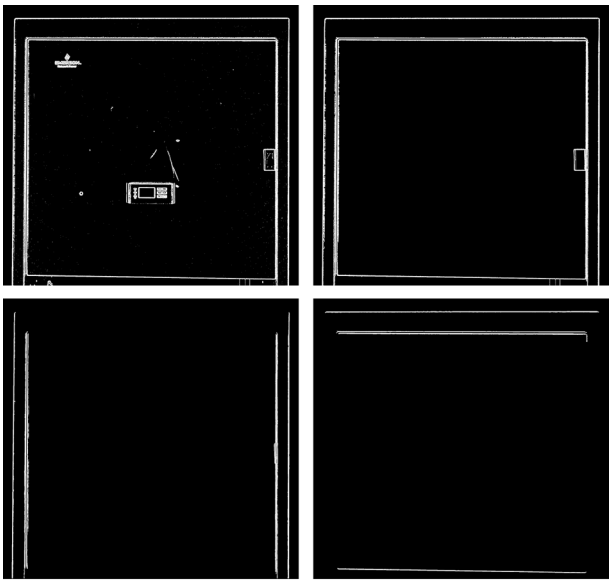

FIGURE 5. Boundary edge extraction based on image morphological operations.

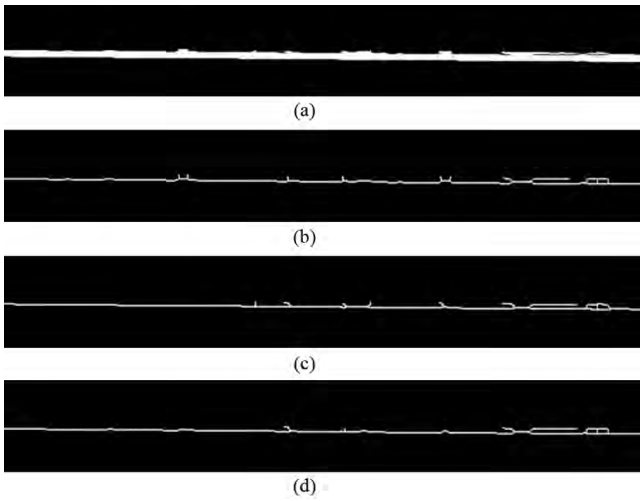

FIGURE 6. Boundary skeleton extraction results by different image tinning algorithms: (a) ROI, (b) OPTA, (c) K3M, and (d) Zhang-Suen.

features are used to indicate that defects are present. This is because the image moment features can be used to describe the image morphologies like size, shape and gray scale, which are not affected by illumination, noise and deformation. In order to detect the defects, extracted boundary images are first divided into smaller image blocks due to the boundary length (larger than 1000 pixels) is much higher than its width (less than 10 pixels). Then anomaly features of abnormal image blocks are determined. Finally, boundary defect inspection is conducted by Gaussian distribution modeling to determine if the image blocks are abnormal.

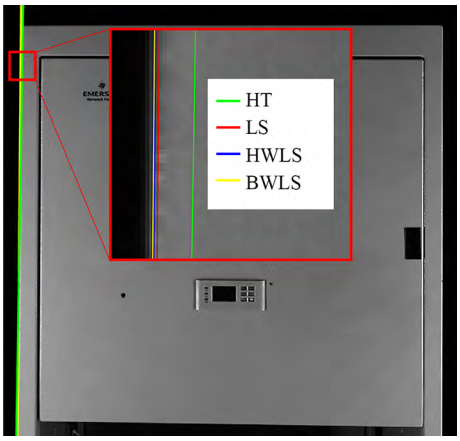

FIGURE 7. Fitting lines obtained with the HT, the LS, the HWLS, and the BWLS algorithms.

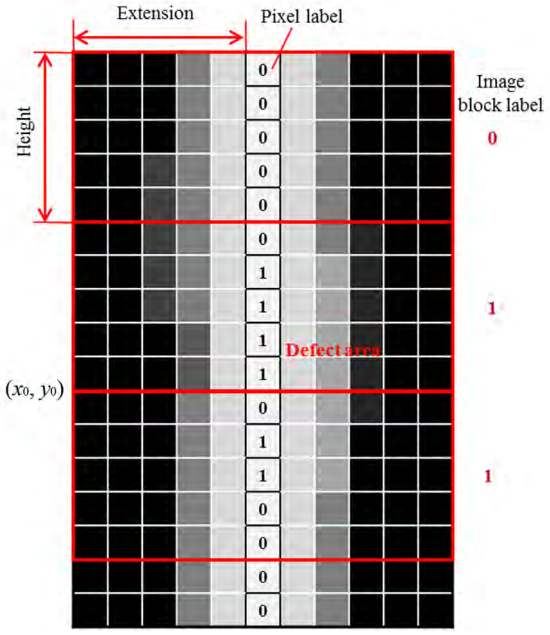

FIGURE 8. The schematic diagram of dividing the boundary image into smaller blocks.

A. IMAGE BLOCK PARTITIONING

Figure 8 shows the schematic diagram of dividing the boundary image into smaller blocks. The boundary width is firstly expanded to $2e + 1$ pixels taking the boundary center line as the axis of symmetry and e is the size of extension. The extended boundary image is then divided into smaller block with the same height h. Image blocks of horizontal boundaries are further rotated 90 degrees to align with vertical boundaries.

The partitioned image block $B(x, y)$ can be expressed by

$$B(x, y) = f(x_0 + x, y_0 + y), x \in [0, 2e], y \in [0, h - 1] \quad (1)$$

where x_0 and y_0 are the original coordinates of the partitioned image blocks shown in Figure 8, and the size of the $B(x, y)$ is

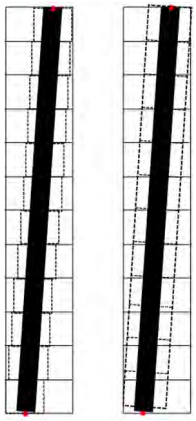

FIGURE 9. The correction of image block partitioning based on image interpolation.

$(2e + 1) \times h$. The pixels of defects are labeled with "1", and the others are labeled with "0". Assuming that the starting pixel coordinate is (x_b, y_b), and the ending pixel coordinate is (x_e, y_e).

$$N_B = \lfloor \frac{y_e - y_b}{h} \rfloor \quad (2)$$

where N_B is the number of image blocks, which is equal to the ratio between boundary length and image block height, and N_B is an integer.

In practice, the boundaries are not absolutely vertical and horizontal, but are affected by product translocation operations and image distortions, leading to horizontal uncertainty. To deal with this problem, an interpolation is used to reduce the error in image block partitioning. The nearest neighbor interpolation and the bilinear interpolation are two commonly used image interpolation methods. Moreover, the bilinear interpolation method is an improved algorithm of the nearest interpolation method. The former is then adopted to correct errors of image block partitioning, and the result is shown in Figure 9.

Furthermore, appropriate partitioning of the image blocks is crucial to ensure the accuracy of defect detection. In this work, the image block size is determined by the correlation between the longitudinal axis of its gray area (R_a) and its label. The higher correlation, the more suitable image block is obtained. As shown in Figure 8, the image block is labeled "0" if all the labeled pixels in the image block are marked "0" ($l_{patch} = 0$), otherwise, the image blocks are marked "1" ($l_{patch} = 1$). The Pearson correlation coefficient [28] is used here to characterize the correlation coefficient between two parameters, which is expressed by

$$r = \frac{\sum_{i=1}^{N}(l_{patch}(i) - \mu_{patch})(R_a(i) - \mu_{Ra})}{\sqrt{\sum_{i=1}^{N}(l_{patch}(i) - \mu_{patch})^2}\sqrt{\sum_{i=1}^{N}(R_a(i) - \mu_{Ra})^2}} \quad (3)$$

where $r \in [-1, 1]$ is the Pearson correlation coefficient;

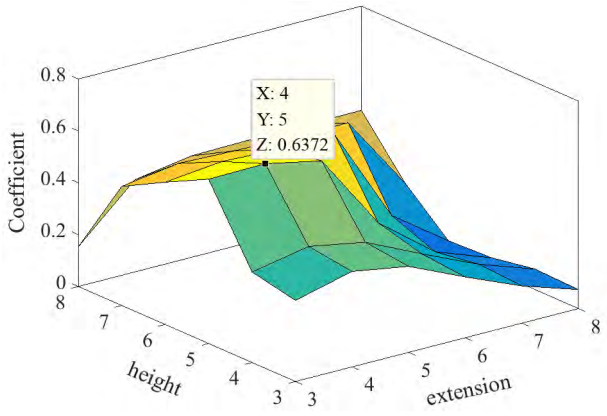

FIGURE 10. Correlation coefficients between different image block heights and extensions.

$l_{patch}(i)$ and $R_a(i)$ are the label and R_a values of the i-th image block respectively; μ_{patch} is the mean value of all pixel labels; μ_{Ra} is the mean value of all image block labels.

In this work, the cabinet boundary center mainly contains three pixels and thus the image block height and extension are set to $3 \sim 8$ pixels. The correlation coefficients between different h and e are shown in Figure 10. It can be seen that the coefficient is the highest (0.6372) when $h = 5$ and $e = 4$. In this case, the correspondingly partitioned image blocks are more suitable for defect detection.

Figure 11 shows the influences of image block size on defect detection accuracy. As shown in Figure 11(a), for $e = 4$, R_a fluctuates when $h = 3$, and the detection of small defects is affected by image texture and noise; despite the fact that Ra changes slowly when $h = 7$, it is still difficult to identify small defects. When $h = 5$, the curve shows larger changes among small defects, image texture and noises, which is more suitable for defect detection. As shown in Figure 11(b), for $h = 5$, several defects are missed by monitoring the changes of Ra when $e = 2$. If $e = 6$, the image background may be regarded as a boundary region, resulting in detecting errors. It can be seen that more accurate reflection of defects can be obtained when $e = 4$ as compared with the other two conditions.

B. ANOMALY FEATURE DETERMINATION OF ABNORMAL IMAGE BLOCKS

Distinguishing the abnormal image blocks with defects from the normal image blocks without defects is the basic objective of boundary defect inspection. Geometrics, projection profiles and gray scales are the fundamental characteristics of images. All image blocks of the cabinet boundary are of the same sizes, making geometrics such as area, length and roundness unsuitable to reflect their differences. Moreover, projection profiles are unable to provide the image feature distribution. In contrast, the gray distribution about gradient and intensity will exhibit noticeable changes if defects appear on the image blocks. On the other hand, intensity statistics including mean, and variance need to be further considered for the best indicator in defect identification.

Kurtosis is a characteristic parameter measuring the probability distribution of random variable, which is used to reflect the non-uniformity of statistical samples [29]. It is considered in order to determine the best indicator. This is because the abnormal image blocks are in a random distribution, which is caused by the differences between defect types.

To calculate the kurtosis of sample feature sequence x_i, the standard deviation of x_i is normalized.

$$z_i = \frac{x_i - \mu}{\sigma}, \quad 1 \le i \le N \tag{4}$$

where z_i is the normalized standard deviation, μ is the mean value and σ is the standard deviation. Based on this, the kurtosis K can be calculated by [29]

$$K = \frac{1}{N}\sum_{i=1}^{N} z_i^4 \tag{5}$$

Equation (5) is used to obtain kurtoses of the long axis of gray area, short axis of gray area (R_b), angle of gray scale (*Phi*), mean gray value (*Mean*), gray deviation (*Deviation*), gray anisotropy (*Anisotropy*) and gray entropy (*Entropy*) of image blocks, results are shown in Figure 12. It can be seen that the *Ra* kurtosis is highest compared to other parameters. Though the *Mean* kurtosis is the second highest value, it is sensitive to illumination conditions. Therefore, R_a is adopted as the anomaly feature that reveals abnormal image blocks with defects.

The R_a of an image block $B(x, y)$ can be calculated by utilizing the image moment ($m_{p,q}$) that is defined as [30]

$$m_{p,q} = \sum_x \sum_y x^p y^q B(x, y) \tag{6}$$

where p and q denote the gray scale moment orders in x and y axes respectively; the order of ($m_{p,q}$) is equal to the sum of p and q.

The centroid (xc, yc) of an image block is calculated from

$$x_c = \frac{m_{1,0}}{m_{0,0}}, \quad y_c = \frac{m_{0,1}}{m_{0,0}} \tag{7}$$

Then we can obtain the image central moment $\mu_{p,q}$ [31]

$$\mu_{p,q} = \sum_x \sum_y (x - x_c)^p (y - y_c)^q B(x, y) \tag{8}$$

The R_a is equal to that of inertial principle axis, which can be acquired using the second-order image moment

$$R_a = 2\sqrt{\frac{1}{2}(\mu_{2,0} + \mu_{0,2}) + \sqrt{4\mu_{1,1}^2 - (\mu_{2,0} - \mu_{0,2})^2}} \tag{9}$$

C. ABNORMAL IMAGE BLOCK DETECTION BY GAUSSIAN DISTRIBUTION MODELING

Image blocks with defects are regarded as abnormal samples, and a normal sample model should be established accordingly for defect detection. In practices, defects appear in product surfaces occur randomly and obey the Gaussian distribution.

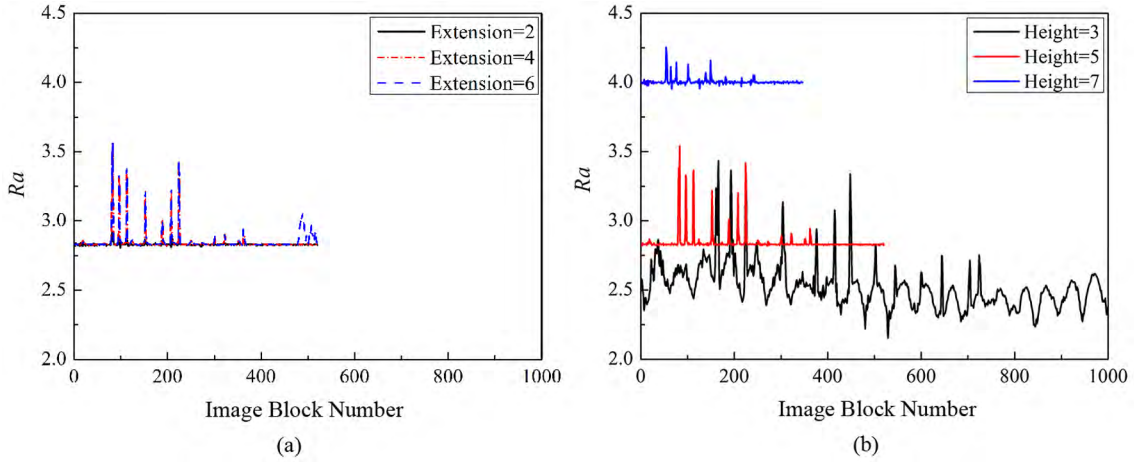

FIGURE 11. Influences of image block size on defect detection accuracy: (a) $e = 4$, the relationship between R_a and h, (b) $h = 5$, the relationship between R_a and e.

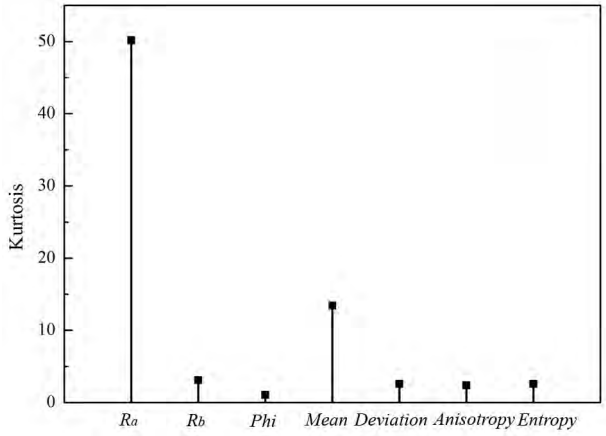

FIGURE 12. Kurtoses of different gray scale parameters.

Hence, it is used to build the normal sample model for defect identification. As mentioned above, the R_a is used as the characterization indicator of image block samples.

Let the normal image block samples be $X = \{x_1, \cdots, x_N\}$. The probability density function p of the samples is

$$p(X, \mu, \sigma) = \frac{1}{\sqrt{2\pi}\sigma} exp(-\frac{(X-\mu)^2}{2\sigma^2}) \tag{10}$$

where μ is the sample mean value and σ is the standard deviation. Accordingly, the maximum likelihood estimate is employed to determine μ and σ. Assuming that samples are mutually independence, and their log-likelihood function $\mathcal{L}$ is [32]

$$\mathcal{L}(X, \mu, \sigma) = -\frac{N}{2}\ln[2\pi] - N\ln[\sigma] - \sum_{n=1}^{N}\frac{(x_n-\mu)^2}{2\sigma^2} \tag{11}$$

Then we have

$$\{\hat{\mu}, \hat{\sigma}\} = \underset{\mu,\sigma}{\text{argmax}}\{\mathcal{L}(X, \mu, \sigma)\} \tag{12}$$

where $\hat{\mu}$ and $\hat{\sigma}$ are the maximum likelihood estimation of μ and σ. The optimal estimated parameters can be obtained when the partial differential of $\mathcal{L}$ is 0, that is,

$$\frac{\partial}{\partial\mu}\mathcal{L}(X, \mu, \sigma) = 0 \tag{13}$$

$$\frac{\partial}{\partial\sigma}\mathcal{L}(X, \mu, \sigma) = 0 \tag{14}$$

Then we have

$$\hat{\mu} = \frac{1}{N}\sum_{n=1}^{N} x_n \tag{15}$$

$$\hat{\sigma}^2 = \frac{1}{N}\sum_{n=1}^{N}(x_n - \hat{\mu})^2 \tag{16}$$

Based on these, the likelihood $\mathcal{L}$ can be calculated. Then the image blocks are labeled. Label "1" indicates that the image block carries defects and others are labeled with "0". That is

$$f(Z) = \begin{cases} 1, & p(Z, \hat{\mu}, \hat{\sigma}) > \theta_p \\ 0, & otherwise \end{cases} \tag{17}$$

where $Z = \{z_1, \cdots, z_M\}$ are the samples that need to be tested, M is the sample number, and θ_p is a threshold.

V. EXPERIMENT

Two experiments were carried out and are presented in this section. The first one aims to determine the optimal illumination condition and its corresponding optimal threshold θ_p for cabinet boundary defect detection. This is because θ_p at different illumination conditions will affect the detection accuracy. Based on the working condition determined, the second experiment was conducted to verify the performance of the proposed method by comparing with other defect inspection approaches.

The image acquisition system shown in Figure 1 is used to capture cabinet surface images. The testing cabinets are

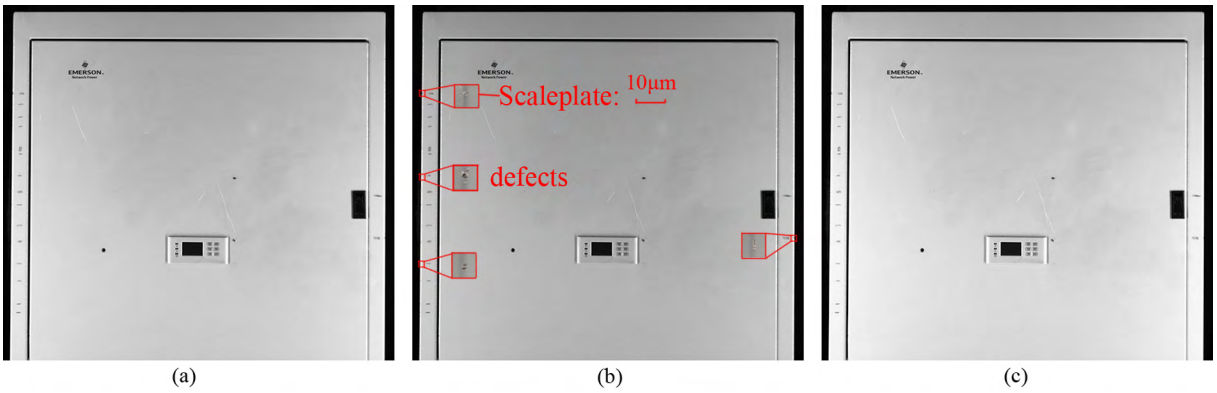

FIGURE 13. Three images of the cabinet illuminated with different lighting intensities: (a) normal lighting, (b) dim lighting, and (c) strong lighting.

illuminated with different conditions including normal lighting, dim lighting and strong lighting. Twenty-one cabinet surface images are captured at the resolution of 2748 × 3840 pixels, and three typical images containing four defect samples captured under different lighting intensities are shown in Figure 13. As can be seen, the defects larger than 2 mm are regarded as the detected objects. All the images are divided into 38961 image blocks. Among these images, 1557 image blocks without defects are used for normal sample model training and the others are used as testing samples.

A. EXPERIMENT 1: OPTIMAL PARAMETERS DETERMINATION

The receiver operating characteristic (ROC) curve is employed to evaluate the performance of the proposed method. In particular, two indicators, true positive rate (*TPR*) and false positive rate (*FPR*), are respectively used as the horizontal and vertical coordinates of the ROC curve. *TPR* represses the probability of truth normal image blocks among those detected as normal image blocks. *FPR* denotes the ratio of truth normal image blocks among those judged as abnormal image blocks. Their expressions are

$$TPR = \frac{TP}{TP + FN} \tag{18}$$

$$FPR = \frac{FP}{FP + TN} \tag{19}$$

where *TP* is the number of defect image blocks that are correctly detected; *FN* is the number of defect image blocks that are mis-detected; *FP* is the number of non-defect image blocks that are mis-judged as defect blocks; *TN* is the number of non-defect image blocks that are correctly detected.

Values of *FPR* and *TPR* are changed with threshold σ_p, and the area under the ROC curve (AUC) can reveal the identification accuracy. The AUC value is in the range of [0, 1]. The higher value indicates higher accuracy, when AUC = 1, *TPR* = 100% and *FPR* = 0%. Figure 14 shows the ROC curves according to different illumination intensities. It can be seen that AUC values vary in the range

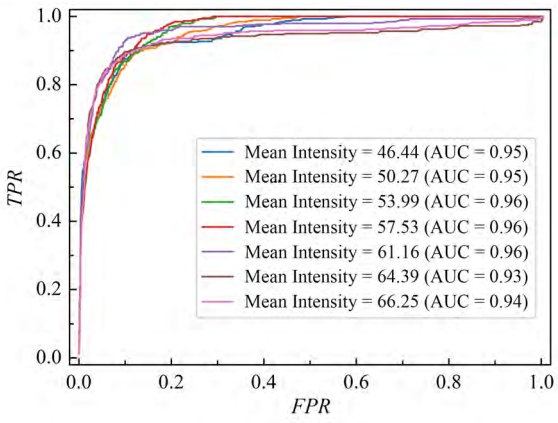

FIGURE 14. The ROC curves according to different light intensities and the corresponding AUC values.

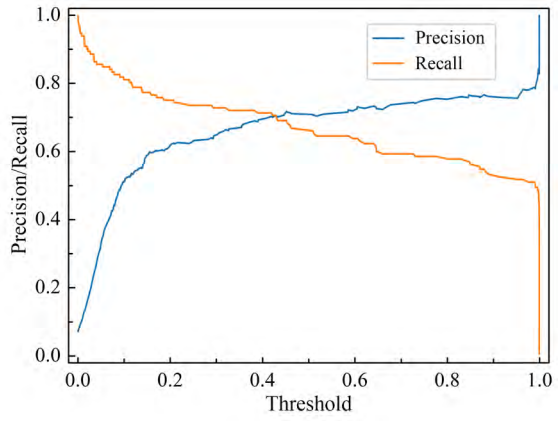

FIGURE 15. The P-R curve according to ROC when mean intensity is 61.16 as shown in Figure 14.

[0.93, 0.96] when the mean illumination intensities change from 46.44 to 66.25. This indicates that the proposed defect inspection method is capable to resist the influence of uneven illumination.

It also can be found from Figure 14 that the rise of the ROC curves increases with increasing light intensities when

TABLE 1. Statistical accuracy of four detection algorithms shown in Figure 16 and Figure 17.

Accuracy	IMA-GM		LR		SVM		NN	
	Training	Testing	Training	Testing	Training	Testing	Training	Testing
$Precision$	0.778	1.000	0.778	0.750	0.722	0.700	0.824	0.714
$Recall$	1.000	0.786	1.000	0.429	0.929	0.500	1.000	0.357
$F-measure$	0.875	0.880	0.875	0.545	0.813	0.583	0.903	0.467

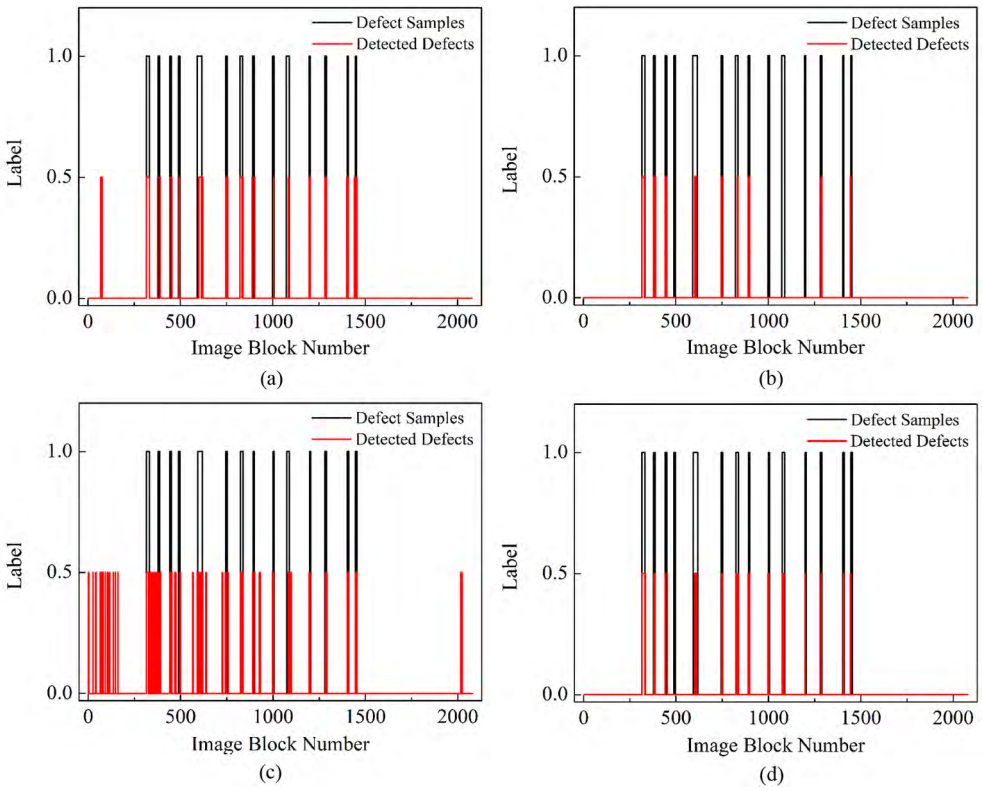

FIGURE 16. Training results of the image block samples using four detection methods: (a) IMA-GM, (b) LR, (c) SVM, and (d) NN.

the *FPR* is less than 20%; afterwards, the ROC curves tend to be saturated. In the saturation region, the *TPR* is smaller when the illumination intensity is higher. Therefore, the optimal light intensity can be determined according to the working conditions and requirements, and in the current work the selected mean intensity is 61.16 and its corresponding AUC value is 0.96.

The next step is to determine the optimal threshold σ_p for the defect detection on image blocks. For this purpose, the precision-recall (P-R) curve is applied. The Precision and Recall are expressed by

$$Precision = \frac{TP}{TP + FP} \tag{20}$$

$$Recall = \frac{TP}{TP + FN} \tag{21}$$

According to the ROC curve depicted in Figure 14 when the mean intensity is 61.16, the P-R curve is obtained and shown in Figure 15. The intersection of the *Precision* curve and *Recall* curve can be defined as the optimal detection threshold, that is, $\theta_p = 0.4305$. Based on the optimal illumination intensity and threshold determined, the accuracy of defect detection is improved.

B. EXPERIMENT 2: COMPARATIVE TEST USING DIFFERENT DEFECT DETECTION ALGORITHMS

The performance of the proposed method, image moment anomaly detection based on Gaussian distribution model (IMA-GM), is evaluated by comparing with three common supervised classification algorithms, logistic regression (LR) [33], support vector machine (SVM) [34] and neural network (NN) [35]. In particular, LR is based on L_2 regularization and its penalty coefficient is set to 10^{-5}; the kernel function of SVM is a radial basis function and its kernel factor is 10; the NN has three layers and the node number of input, hidden and output layers are 32, 64 and 32 respectively, and the Sigmoid activation function is used.

There are 2600 image blocks used in this comparative experiment. Among these images blocks, 2080 blocks are

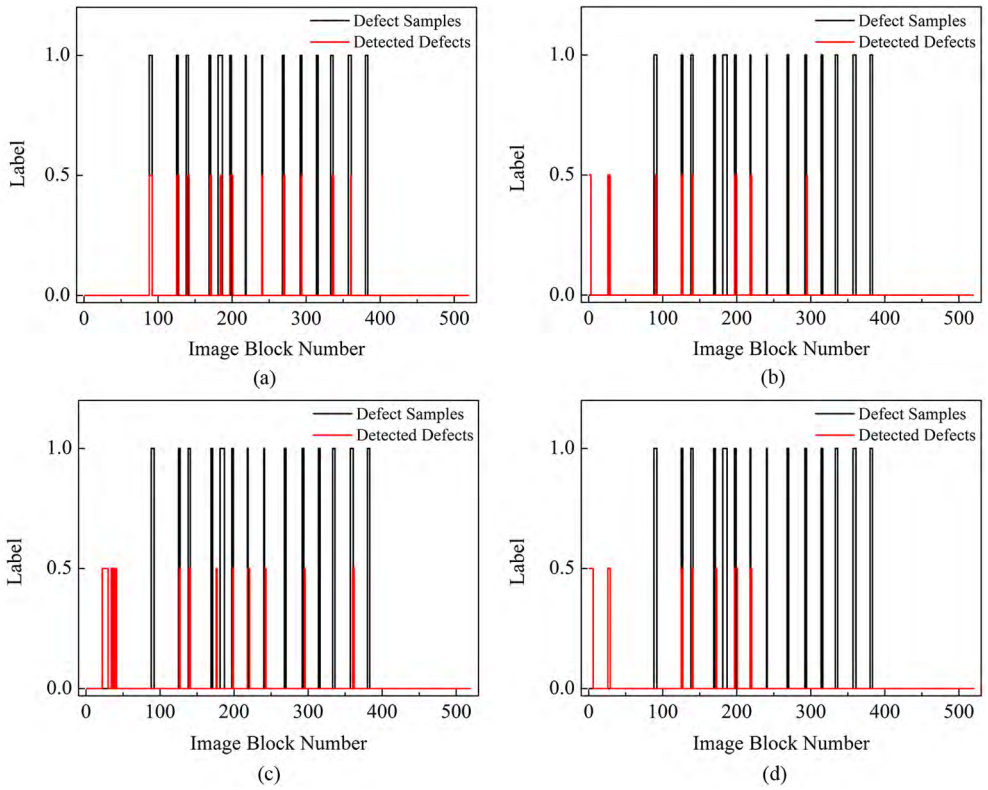

FIGURE 17. Testing results of the image block samples using four detection methods: (a) IMA-GM, (b) LR, (c) SVM, and (d) NN.

used as training samples and 520 image blocks as testing samples. All the image blocks are manually labeled with "0" and "1". Whereas, the identified defects using classification algorithms are labeled with "0.5" in order to differentiate from the manual labels. Training and testing results using the above mentioned four detection methods are shown in Figure 16 and Figure 17 respectively. It needs to be mentioned that the number of image blocks with defects does not equal to the number of defects on the cabinet boundaries because a defect may be divided into different continual parts. This experiment aims to determine whether the product boundaries have defects for quality inspection instead of identifying defect types and severities. Therefore, any one of the continual image blocks is detected as defect sample, it means that the defect is correctly identified.

It can be seen that there are 14 defect samples in the 2080 training samples, and the training results of four algorithms show errors at different levels. As shown in Figures 16(a) and 16(c), all defect samples are correctly detected using the IMA-GM and SVM algorithms. However, one normal sample and eleven normal samples are mis-identified as defect sample using the IMA-GM and SVM algorithms respectively. As shown in Figures 16(b) and 16(d), there are no mis-identified normal sample arising from the LR and NN algorithms. However, five defect samples and one defect sample are not detected using the LR and NN algorithms respectively.

From Figure 17, it also can be found that there are 14 defect samples in the 520 testing samples. Compared with other three methods, the IMA-GM method only mis-detected three defect samples. The LR algorithm not only mis-detected eight defect samples but also mis-judged two normal samples. Similarly, The SVM mis-detected seven defect samples and mis-judged three normal samples. The NN mis-detected six defect samples but also mis-judged two normal samples.

For further comparative analysis, TABLE 1 displays the accuracy indicators of *Precision*, *Recall* and *F-measure* calculated based on the actual defect quantity and locations, and it is expressed as

$$F\text{-}measure = \frac{2Precision \times Recall}{Precision + Recall} \tag{22}$$

As shown in TABLE 1, the *F-measure* values of the training results of four algorithms are similar and they are 0.875, 0.875, 0.813 and 0.903 respectively. On the other hand, the *F-measure* (0.880) of sample testing using IMA-GM is higher than that of other three methods (LR 0.545, SVM 0.583, NN 0.467). Based on the comparative analysis, the proposed image moment anomaly based defect inspection is more suitable for cabinet boundary defect detection.

VI. CONCLUSION

Aiming to solve the problem of production defect detection on electric distribution cabinet boundaries, a new approach of boundary defect inspection based on image moment feature anomaly is proposed. The boundary areas are extracted from cabinet surface images and then divided into smaller image blocks. The anomaly features of image blocks are acquired and used to identify the abnormal image blocks with defects. Based on this, the boundary defects are detected. The main conclusions are:

1) The Gaussian distribution model of image blocks is established based on the fact that cabinet surface defects appear randomly. Furthermore, the probability density function is employed to distinguish the normal and abnormal image blocks. For cabinet quality inspection, the optimal illumination intensity is 61.16 and the optimal probability density threshold θ_p is 0.4305, and the corresponding AUC of the ROC curve is 0.96.
2) Based on labeled sample training, the detection accuracy, *F-measure*, of the proposed method IMA-GM can reach 0.880, which is higher than that of LR (0.545), SVM (0.583) and NN (0.467). This indicates that the proposed method is more suitable for the cabinet boundary defect detection than other three algorithms.
3) The gray scale longitudinal axis of image blocks is recommended as the anomaly feature for abnormal image block identification because its kurtosis value is higher than that of gray mean value, gray variance and gray scale latitudinal axis.

Future work will be focused on the acquisition of defect samples and the optimization of the training model to improve the accuracy of defect detection.

REFERENCES

[1] L. Qiu, X. Wu, and Z. Yu, "A high-efficiency fully convolutional networks for pixel-wise surface defect detection," *IEEE Access*, vol. 7, pp. 15884–15893, 2019.

[2] D. Carrera, F. Manganini, G. Boracchi, and E. Lanzarone, "Defect detection in SEM images of nanofibrous materials," *IEEE Trans. Ind. Inform.*, vol. 13, no. 2, pp. 551–561, Apr. 2017.

[3] H. Feng, Z. Jiang, F. Xie, P. Yang, J. Shi, and L. Chen, "Automatic fastener classification and defect detection in vision-based railway inspection systems," *IEEE Trans. Instrum. Meas.*, vol. 63, no. 4, pp. 877–888, Apr. 2014.

[4] H. Chen, Y. Cui, R. Qiu, P. Chen, W. Liu, and K. Liu, "Image-alignment based matching for irregular contour defects detection," *IEEE Access*, vol. 6, pp. 68749–68759, 2018.

[5] L. Jia, Z. Junguo, S. Chen, and Z. Hou, "Fabric defect inspection based on lattice segmentation and lattice templates," *J. Franklin Inst.*, vol. 355, no. 15, pp. 7764–7798, 2018.

[6] D.-M. Tsai and D. E. R. Molina, "Morphology-based defect detection in machined surfaces with circular tool-mark patterns," *Measurement*, vol. 134, pp. 209–217, Feb. 2019.

[7] L. Zhang, L. Zhang, B. Du, J. You, and D. Tao, "Hyperspectral image unsupervised classification by robust manifold matrix factorization," *Inf. Sci.*, vol. 485, pp. 154–169, Jun. 2019.

[8] Q. Huangpeng, H. Zhang, X. Zeng, and W. Huang, "Automatic visual defect detection using texture prior and low-rank representation," *IEEE Access*, vol. 6, pp. 37965–37976, 2018.

[9] M. H. Karimi and D. Asemani, "Surface defect detection in tiling industries using digital image processing methods: Analysis and evaluation," *ISA Trans.*, vol. 53, no. 3, pp. 834–844, 2014.

[10] Y. Li, W. Zhao, and J. Pan, "Deformable patterned fabric defect detection with fisher criterion-based deep learning," *IEEE Trans. Autom. Sci. Eng.*, vol. 14, no. 2, pp. 1256–1264, Apr. 2017.

[11] K. Liu, H. Wang, H. Chen, E. Qu, Y. Tian, and H. Sun, "Steel surface defect detection using a new Haar–weibull-variance model in unsupervised manner," *IEEE Trans. Instrum. Meas.*, vol. 66, no. 10, pp. 2585–2596, Oct. 2017.

[12] X. Bai, Y. Fang, W. Lin, L. Wang, and B.-F. Ju, "Saliency-based defect detection in industrial images by using phase spectrum," *IEEE Trans. Ind. Informat.*, vol. 10, no. 4, pp. 2135–2145, Nov. 2014.

[13] L. Zhang, Q. Zhang, B. Du, X. Huang, Y. Y. Tang, and D. Tao, "Simultaneous spectral-spatial feature selection and extraction for hyperspectral images," *IEEE Trans. Cybern.*, vol. 48, no. 1, pp. 16–28, Jan. 2018.

[14] L. Jia, C. Chen, J. Liang, and Z. Hou, "Fabric defect inspection based on lattice segmentation and Gabor filtering," *Neurocomputing*, vol. 238, pp. 84–102, May 2017.

[15] W. C. Li and D. M. Tsai, "Defect inspection in low-contrast LCD images using Hough transform-based nonstationary line detection," *IEEE Trans. Ind. Informat.*, vol. 7, no. 1, pp. 136–147, Feb. 2011.

[16] W. Zhou, M. Fei, H. Zhou, and K. Li, "A sparse representation based fast detection method for surface defect detection of bottle caps," *Neurocomputing*, vol. 123, pp. 406–414, Jan. 2014.

[17] X.-C. Yuan, L.-S. Wu, and Q. Peng, "An improved Otsu method using the weighted object variance for defect detection," *Appl. Surf. Sci.*, vol. 349, pp. 472–484, Sep. 2015.

[18] G. Cao, S. Ruan, Y. Peng, S. Huang, and N. Kwok, "Large-complex-surface defect detection by hybrid gradient threshold segmentation and image registration," *IEEE Access*, vol. 6, pp. 36235–36246, 2018.

[19] P. Li and H. Xiao, "An improved filtering method for quantum color image in frequency domain," *Int. J. Theor. Phys.*, vol. 57, no. 1, pp. 258–278, 2018.

[20] L. Xiao, C. Li, Z. Wu, and T. Wang, "An enhancement method for X-ray image via fuzzy noise removal and homomorphic filtering," *Neurocomputing*, vol. 195, pp. 56–64, Jun. 2016.

[21] P. K. Saha, G. Borgefors, and G. S. di Baja, "A survey on skeletonization algorithms and their applications," *Pattern Recognit. Lett.*, vol. 76, pp. 3–12, Jun. 2016.

[22] W. Deng, S. S. Iyengar, and N. E. Brener, "A fast parallel thinning algorithm for the binary image skeletonization," *Int. J. High Perform. Comput.*, vol. 14, no. 1, pp. 65–81, 2000.

[23] K. Saeed, M. Tabedzki, M. Rybnik, and M. Adamski, "K3M: A universal algorithm for image skeletonization and a review of thinning techniques," *Int. J. Appl. Math. Comput. Sci.*, vol. 20, no. 2, pp. 317–335, 2010.

[24] T. Y. Zhang and C. Y. Suen, "A fast parallel algorithm for thinning digital patterns," *Commun. ACM*, vol. 27, no. 3, pp. 236–239, 1984.

[25] K. J. Choi, Y. H. Lee, J. W. Moon, C. K. Park, and F. Harashima, "Development of an automatic stencil inspection system using modified Hough transform and fuzzy logic," *IEEE Trans. Ind. Electron.*, vol. 54, no. 1, pp. 604–611, Feb. 2007.

[26] S. Zhang, H. Zhou, F. Jiang, and X. Li, "Robust visual tracking using structurally random projection and weighted least squares," *IEEE Trans. Circuits Syst. Video Technol.*, vol. 25, no. 11, pp. 1749–1760, Nov. 2015.

[27] C. Yu and W. Yao, "Robust linear regression: A review and comparison," *Commun. Statist.-Simul. Comput.*, vol. 46, no. 8, pp. 6261–6282, 2017.

[28] Q. Zou, J. Zeng, L. Cao, and R. Ji, "A novel features ranking metric with application to scalable visual and bioinformatics data classification," *Neurocomputing*, vol. 173, pp. 346–354, Jan. 2016.

[29] C. C. Aggarwal, *Outlier Analysis*. New York, NY, USA: Springer, 2013.

[30] E. G. Karakasis, A. Amanatiadis, A. Gasteratos, and S. A. Chatzichristofis, "Image moment invariants as local features for content based image retrieval using the bag-of-visual-words model," *Pattern Recognit. Lett.*, vol. 55, pp. 22–27, Apr. 2015.

[31] G. Coatrieux, H. Huang, H. Shu, L. Luo, and C. Roux, "A watermarking-based medical image integrity control system and an image moment signature for tampering characterization," *IEEE J. Biomed. Health Inform.*, vol. 17, no. 6, pp. 1057–1067, Nov. 2013.

[32] J. M. Guo, H. Prasetyo, M. E. Farfoura, and H. Lee, "Vehicle verification using features from curvelet transform and generalized Gaussian distribution modeling," *IEEE Trans. Intell. Transp. Syst.*, vol. 16, no. 4, pp. 1989–1998, Aug. 2015.

[33] T. Kim and S. Wright, "PMU placement for line outage identification via multinomial logistic regression," *IEEE Trans. Smart Grid*, vol. 9, no. 1, pp. 122–131, Jan. 2018.

[34] F. Luo, B. Du, L. Zhang, L. Zhang, and D. Tao, "Feature learning using spatial-spectral hypergraph discriminant analysis for hyperspectral image," *IEEE Trans. Cybern.*, to be published. doi: 10.1109/TCYB.2018.2810806.
[35] L. Wang *et al.*, "Accelerating nearest neighbor partitioning neural network classifier based on CUDA," *Eng. Appl. Artif. Intell.*, vol. 68, pp. 53–62, Feb. 2018.

YEPING PENG received the B.Sc. degree in mechanical design, manufacture, and automation from Harbin Engineering University, China, in 2011, and the M.Sc. and Ph.D. degrees in mechanical engineering from Xi'an Jiaotong University, China, in 2014 and 2017, respectively. She is currently an Assistant Professor with the Shenzhen Key Laboratory of Electromagnetic Control, College of Mechatronics and Control Engineering, Shenzhen University, China. Her main research interests include machine vision, image processing, and information processing.

SONGBO RUAN received the B.Sc. degree in intelligence science and technology from South Central University for Nationalities, China, in 2016. He is currently pursuing the master's degree in control science and engineering with the Shenzhen Key Laboratory of Electromagnetic Control, Shenzhen University, China. His research interests include machine vision and information processing.

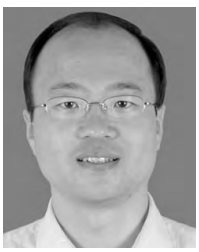

GUANGZHONG CAO received the B.Sc., M.Sc., and Ph.D. degrees in electrical engineering and automation from Xi'an Jiaotong University, China, in 1989, 1992, and 1996, respectively. He is currently a Professor and the Director of the Shenzhen Key Laboratory of Electromagnetic Control, Shenzhen University, China. He has authored more than 80 articles published in refereed journals and conference proceedings. His research interests include control theory, robotic technology, machine vision, and information processing.

SUDAN HUANG received the B.Sc. and M.Sc. degrees in control theory and control engineering from Shenzhen University, China, in 2009 and 2012, respectively, and the Ph.D. degree in electrical engineering from Southwest Jiaotong University, China. She is currently an Assistant Professor with the Shenzhen Key Laboratory of Electromagnetic Control, College of Mechatronics and Control Engineering, Shenzhen University. Her research interests include information processing, control theory, and its applications.

NGAIMING KWOK received the B.Sc. degree in computer science from the University of East Asia, Macau, the M.Sc. degree in control engineering from The Hong Kong Polytechnic University, Hong Kong, and the Ph.D. degree in mobile robotics from the University of Technology Sydney, Australia, in 1993, 1997, and 2006, respectively. He is currently a Lecturer with the School of Mechanical and Manufacturing Engineering, The University of New South Wales, Sydney, Australia. He has published more than 150 journal articles and conference papers. His research interests include intelligent computation, image processing, and automatic control.

SHENGXI ZHOU received the B.Sc. degree in mechanical design, manufacturing and automation from Southwest University, China, in 2010, and the M.Sc. and Ph.D. degrees in mechanical engineering from Xi'an Jiaotong University, China, in 2013 and 2016, respectively. In 2017, he was a Postdoctoral Associate with Virginia Polytechnic Institute and State University (Virginia Tech), USA. He is currently a Professor with the School of Aeronautics, Northwestern Polytechnical University, China. His main research interests include energy harvesting, nonlinear vibration, and system identification.